THE JOURNAL OF PHYSICAL CHEMISTRY A

Article

pubs.acs.org/JPCA

Molecular Aluminum Additive for Burn Enhancement of Hydrocarbon Fuels

Philip M. Guerieri,[†] Samantha DeCarlo,[†] Bryan Eichhorn,[†] Terrence Connell,[‡] Richard A. Yetter,[‡] Xin Tang,[§] Zachary Hicks,[§] Kit H. Bowen,[§] and Michael R. Zachariah*[,†]

[†]University of Maryland, College Park, Maryland 20740, United States

[‡]The Pennsylvania State University, University Park, Pennsylvania 16801, United States

[§]Johns Hopkins University, Baltimore, Maryland 21218, United States

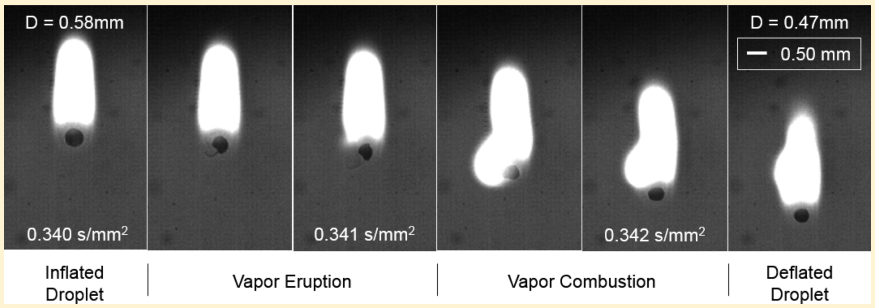

ABSTRACT: Additives to hydrocarbon fuels are commonly explored to change the combustion dynamics, chemical distribution, and/or product integrity. Here we employ a novel aluminum-based molecular additive, Al(I) tetrameric cluster $[AlBrNEt_3]_4$ (Et = C_2H_5), to a hydrocarbon fuel and evaluate the resultant single-droplet combustion properties. This Al_4 cluster offers a soluble alternative to nanoscale particulate additives that have recently been explored and may mitigate the observed problems of particle aggregation. Results show the $[AlBrNEt_3]_4$ additive to increase the burn rate constant of a toluene−diethyl ether fuel mixture by ∼20% in a room temperature oxygen environment with only 39 mM of active aluminum additive (0.16 wt % limited by additive solubility). In comparison, a roughly similar addition of nano-aluminum particulate shows no discernible difference in burn properties of the hydrocarbon fuel. High speed video shows the $[AlBrNEt_3]_4$ to induce microexplosive gas release events during the last ∼30% of the droplet combustion time. We attribute this to HBr gas release based on results of temperature-programmed reaction (TPR) experiments of the $[AlBrNEt_3]_4$ dosed with O_2 and D_2O. A possible mechanism of burn rate enhancement is presented that is consistent with microexplosion observations and TPR results.

INTRODUCTION

With their high density-specific enthalpy of combustion, energetic metals can be added to propellants and explosives to drastically increase the volumetric energy density as evidenced in Figure 1. Historically, micron-sized metal particles have been studied and used in rocket propellant formulations as either the primary fuel (e.g., solid composite rocket propellants) or as an additive to increase the energy content of solid and gelled propellants. The particle size of these additives has a significant effect on the observed energetic benefit. In particular, metal nanoparticles (with diameters between 1 and 100 nm) have demonstrated shorter ignition delays and higher burning rates than larger particles due to their increasing surface-to-volume ratio as particle size decreases.[1] Nanoscale metal additives are also better suited to liquid propellant incorporation since they can replace traditionally nonenergetic gelling agents and boast lower settling velocities than larger particles. However, nanoscale additives introduce new challenges. Increasing reactivity with decreasing particle size has a lower limit of potential activity because the inert native oxide on the metal particle surface comprises an increasing mass fraction of the material as the particle size decreases.[1] Colloidal stability also remains a significant

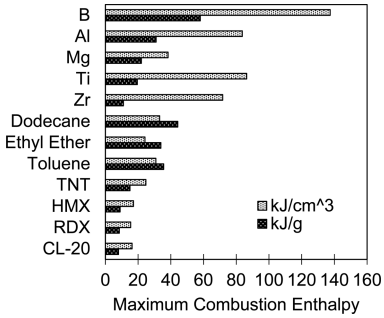

Figure 1. Volume and mass specific maximum combustion enthalpies for select energetic metals, liquid fuels, and explosives.[2]

Received: September 2, 2015
Revised: October 21, 2015
Published: October 21, 2015

DOI: 10.1021/acs.jpca.5b08580
J. Phys. Chem. A 2015, 119, 11084−11093

challenge as nanoparticles are highly prone to aggregate and settle out of suspension before the reactive benefits of the additive can be utilized.[1]

Nanoparticles can be dispersed in liquids by repulsive electrostatic forces and Brownian motion creating a "nanofluid". Research in this area has grown rapidly since first being proposed by Choi in 1995 to increase fluid heat transfer rates.[3] Here we focus on nanostructures as a means to increase energy density or moderate the burning characteristics of traditional liquid fuels ("nanofuels").

Much of the early nanofuel research examined direct use of nanoparticles as diesel fuel additives for compression ignition engines. Various nanoparticle additives were shown to decrease NO_x, hydrocarbon, and/or CO emissions including those of Al,[4−6] Al_2O_3,[5] Fe,[6] B,[6] CeO_2,[7] Fe_3O_4,[8] and carbon nanotubes (CNT).[9] Jet fuels, monopropellants, and other hydrocarbons as the base liquid fuel have also received increased research attention concurrently with diesel.[10−25] Metal oxide particles have been shown to participate directly or catalytically in the oxidation of JP-10 in an atomized flow reactor,[10] and nAl reduced the apparent ignition delay of JP-8 in a rapid compression machine.[11] Efforts with nitromethane in pressure vessels have shown increased burn rates with the addition of functionalized graphene sheets,[12] silica,[13,14] AlOOH,[12] Al_2O_3,[14] and nAl.[13,15]

The past decade of emerging research on nanofuel evaporation and combustion demonstrates the promise of adding metals and metal oxides to liquid fuels for increased energy densities, shortened ignition delay times, higher heats of combustion, decreased emissions, and promotion of evaporation and combustion rates. A variety of interacting processes and mechanisms have been proposed and supported by empirical observation in droplet evaporation and combustion studies.[16−25] The most notable mechanisms promoting evaporation and combustion rates include fuel droplet temperature increase by radiative absorption of the additives, physical mixing and eruption of material by microexplosions, and the relatively rare cases of clear simultaneous particle/solvent burning.[16−21] However, nanoparticles also aggregate easily compared to larger particles, thus posing serious problems in nanofuel formulation and combustion. In the former case, physical mixing methods show poor long-term stability of the suspensions as particles aggregate and settle. Chemical stabilization by electrostatic dispersion and surface modification can increase the maximum stable particle loading but can also inhibit combustion of the particles.[1] Even with a stable nanofuel, particle aggregation within the droplets has been shown to occur at a similar time scale of droplet evaporation and burning, in many cases delaying the additive's participation in combustion (by microexplosions or aggregate ignitions) to the late stages of the droplet lifetime and mitigating evaporation or burning rate increases[16,22,19] or even decreasing droplet evaporation rates.[23,24]

Since the precise effects of a particulate additive depend on the relative strength of these competing mechanisms, they are highly dependent on ambient temperature, particle loading, chemical stabilizations used, and the physical characteristics of the pure solvent. Volatility and viscosity for instance will affect the relative time scales of solvent evaporation versus particle transport and aggregation in the fluid. An energetic, soluble alternative to nanoparticle additives has the potential to overcome these aggregation challenges while conserving the benefits of high-energy-density additives, thereby promoting relative dominance of the combustion-promoting mechanisms.

The current study utilizes a novel aluminum-based molecular additive that for the first time enables the investigation of a directly soluble alternative to the nanometal particle dispersions that have previously been examined. The additive is an in-house-synthesized aluminum(I) bromide tetramer stabilized with triethylamine ligands, which was dissolved in a toluene−diethyl ether cosolvent matrix. Droplet combustion with and without the molecular additive was measured in a drop tower to estimate burning rate constants. The additive was further studied by TPR mass spectrometry to probe reaction mechanisms and products. These results were then compared with similar experiments incorporating standard particulate nano-aluminum.

EXPERIMENTAL SECTION

Molecular Additive. The molecular additive used in this work is a hydrocarbon-soluble Al(I) tetrameric cluster, $[AlBrNEt_3]_4$ (Figure 2), synthesized from the $AlBr{\cdot}NEt_3$ starting material produced from a Schnöckel-type metal halide co-condensation reactor (MHCR).[26−28] This tetramer is a ligand-stabilized component of the $AlBr{\cdot}NEt_3$ precursor solution and contains aluminum in the 1+ oxidation state with covalent Al−Al bonds (average bond length 2.41 Å). This product is isolated from solution as a yellow crystalline solid and exhibits good solubility in the nonpolar organic solvents benzene and toluene. To maximize the concentration of aluminum in solution, the donor solvent Et_2O was added to increase solubility through the use of a tol:Et_2O (4:1) cosolvent mixture. This mixture allows for more concentrated samples containing ∼40 mmol of aluminum, compared to ∼24 mmol of aluminum in pure toluene solutions. Two concentrations of $[AlBrNEt_3]_4$ additive in the tol:Et_2O cosolvent were produced and tested to study any significant effects of concentration variation. Because of the low oxidation state of the aluminum(I) tetramer and lack of an oxide passivation layer normally found on bulk aluminum metal, it is extremely air and moisture sensitive. Once an $[AlBrNEt_3]_4$ solution is exposed to air, rapid oxidation occurs causing precipitation of aluminum oxide and hydrolysis products, which necessitates the use of Schlenk techniques and gastight syringes in the combustion studies.

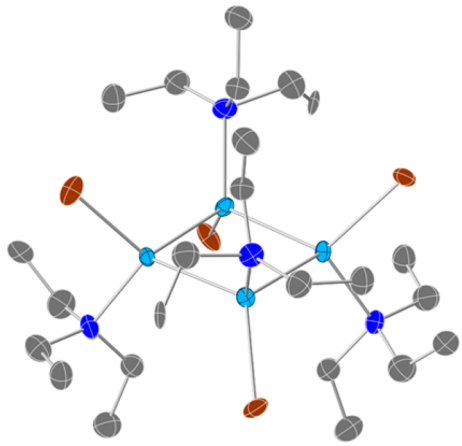

Figure 2. Crystal structure of $[AlBrNEt_3]_4$: Al (light blue), N (dark blue), C (gray), Br (brown); hydrogen atoms were omitted for clarity.

DOI: 10.1021/acs.jpca.5b08580
J. Phys. Chem. A 2015, 119, 11084−11093

The dissolution of the $[AlBrNEt_3]_4$ in the cosolvent matrix (tol:Et_2O) was performed in a glovebox under an Ar atmosphere, and resulted in deep clear yellow solutions. Once completely dissolved, the solutions were then loaded into an Ar-purged gastight syringe. To limit exposure of the sample to air, the syringe is kept in a sealed bag under argon. Prior to being connected to the drop tower, 6 in. of 1/16 in. o.d. × 0.040 in. i.d. PTFE tubing is flushed with nitrogen to prevent oxidation of the product prior to tower introduction.

All reactions are performed under an argon atmosphere in a glovebox or under dry nitrogen using standard Schlenk techniques. Toluene and diethyl ether were purified by distillation from sodium benzophenone ketyl under a dinitrogen atmosphere, and triethylamine was purified through distillation over calcium hydride. All purified solvents were stored in modified Schlenk vessels over 3 Å molecular sieves under an argon atmosphere. The ^1H and ^{13}C NMR spectra were recorded on a Bruker DRX500 Avance spectrometer.

$AlBr{\cdot}(NEt_3)_n$. Aluminum metal (0.8410 g, 31.1 mmol) was reacted with gaseous HBr (36.5 mmol) over 3 h at approximately 1200 K in a modified Schnöckel-type metal halide co-condensation reactor.[26,27] The resultant gas-phase AlBr was co-condensed with a mixture of toluene:triethylamine (3:1 v/v) at approximately 77 K. The solvent matrix was thawed to −80 °C, and the resultant yellow-brown solution stored at that temperature prior to use.[26,27] Titration of the $AlBr{\cdot}(NEt_3)_n$ solution via Mohr's method revealed a bromide concentration of 201 mM yielding an Al:Br ratio of 1:1.10. The $[AlBrNEt_3]_4$ complex was prepared through the use of a slightly modified published procedure[28] as described below.

$[AlBrNEt_3]_4$. A 40 mL aliquot of $AlBr{\cdot}(NEt_3)_n$ was transferred to a Schlenk flask. Approximately 10 mL of solvent was removed *in vacuo* while warming the solution to room temperature. Solvent removal stopped upon observing the formation of yellow solid, which stood at room temperature overnight. The next day the yellow solid was isolated and washed with copious amounts of hexanes, and crystals suitable for X-ray diffraction were obtained. ^1H NMR (500 MHz, tol-d_8): δ (ppm) = 1.18 (t), 3.08 (q) ^{13}C NMR (400 MHz, tol-d_8): δ (ppm) = 9.80, 49.05. The overall yield of $[AlBrNEt_3]_4$, based on the parent solution $AlBr{\cdot}NEt_3$, is up to 20%.

$[AlBrNEt_3]_4$ Solution. In a glovebox, 36.4 mg (0.0437 mmol) of $[AlBrNEt_3]_4$ was dissolved in 3.6 mL of dry toluene. After 20 min, 0.9 mL of dry Et_2O was added to the $[AlBrNEt_3]_4$ solution for a final solution concentration of 9.7 mM $[AlBrNEt_3]_4$. The solution was then taken up in Hamilton Model 1005 SL gastight syringe, which was sealed via a syringe lock. The 5.2 mM sample was prepared in a similar manner utilizing 17.9 mg (0.0215 mmol) of $[AlBrNEt_3]_4$ and was dissolved in 4.5 mL of toluene/Et_2O (4:1) mixture.

Nano-Aluminum Additive. nAl sample preparations begin by adding 2.0 mg/mL of 80 nm (primary particle size) aluminum particles (Novacentrix, Inc., 80% active Al with 2−5 nm oxide shell as confirmed by TEM of as-received particles shown in Figure 3) to the toluene/Et_2O (4:1) solvent mixture. As with the $[AlBrNEt_3]_4$ and control samples, the solvent mixtures are made in small batches for each sample (just before nanoparticle addition in this case) to minimize preferential evaporation of the ether component. The nanoparticles are suspended via an ultrasonication bath for 1 h and allowed to gravitationally settle for 24 h before decanting the stable suspension. By allowing the suspension to stand for 24 h, the largest fractal aggregates settle and are removed from the

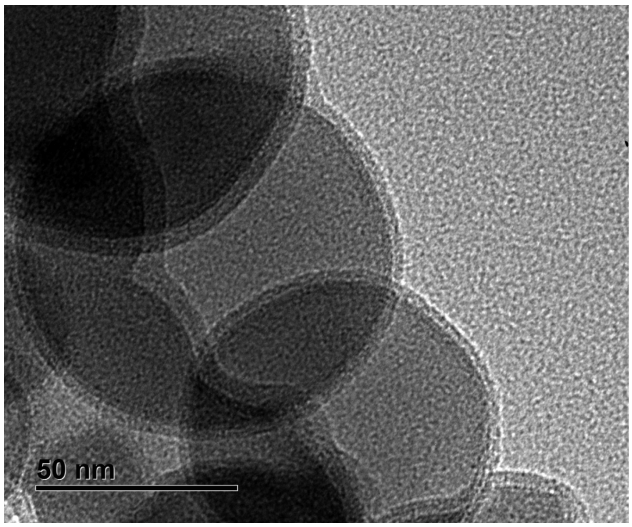

Figure 3. Nano-aluminum particulate additive TEM showing 2−5 nm oxide shell.

formulation to promote suspension stability and prevent needle clogging during experiments. The resultant particle concentration is determined by vacuum drying a known volume of the decantant and weighing the remaining solids. Approximately 4 mL of sample is loaded into a Hamilton Model 1005 SL gastight syringe connected to 6 in. of 1/16 in. o.d. × 0.040 in. i.d. PTFE tubing. Any air is removed from the syringe and tubing before compression-fitting the tubing to the capillary tube/needle assembly and engaging the syringe in the syringe pump.

Combustion Characterization. To evaluate the effect of additives on fuel combustion behavior, we employ a single droplet combustion measurement in a drop tower arrangement depicted in Figure 4. A fuel droplet is generated at the top of a tower in an inert (nitrogen) filled sheath nozzle (Figure 4, point 1) and released to free fall into a room temperature, oxygen-rich environment whereby ignition is initiated as the droplet passes through a small methane pilot flame (point 2). The 20 in. tall, 3 in. square tower is constructed of aluminum with removable transparent windows on three sides (point 3). Oxidizing and carrier gases enter the tower via oxygen flow at 12 LPM diffused and delivered at the top of the tower (point 4) and nitrogen flow at approximately 0.25 LPM flowing through the droplet delivery nozzle (point 5). All gases escape the tower via exhaust at the open bottom into a steel duct (point 6). To ignite the droplets, methane is introduced via two 800 μm o.d. ceramic tubes from opposite sides of the tower at approximately 50 mL/min to create two stable diffusion flames 1.7 cm below the droplet nozzle (point 7).

Droplet generation is achieved with a capillary needle assembly nested in a glass sheath tube supplied with nitrogen gas flow (Figure 4, point 1). The stainless steel needles are assembled by clearance fitting 1.5 in. sections of 0.010 in. o.d./0.005 in. i.d. SS capillary tubing (Microgroup, Inc.) inside of a 7 in. section of 1/16 in. o.d./0.020 in. i.d. SS tube (IDEX Health & Science LLC.). The two sections are sealed together using steel-reinforced epoxy. This design is chosen for disposability of the needles to eliminate the possibility of sample cross-contamination. The final diameter of the needle nested in the nozzle is practically minimized to require the slowest sheath flow to generate a given size droplet. For droplets combusting

DOI: 10.1021/acs.jpca.5b08580
J. Phys. Chem. A 2015, 119, 11084−11093

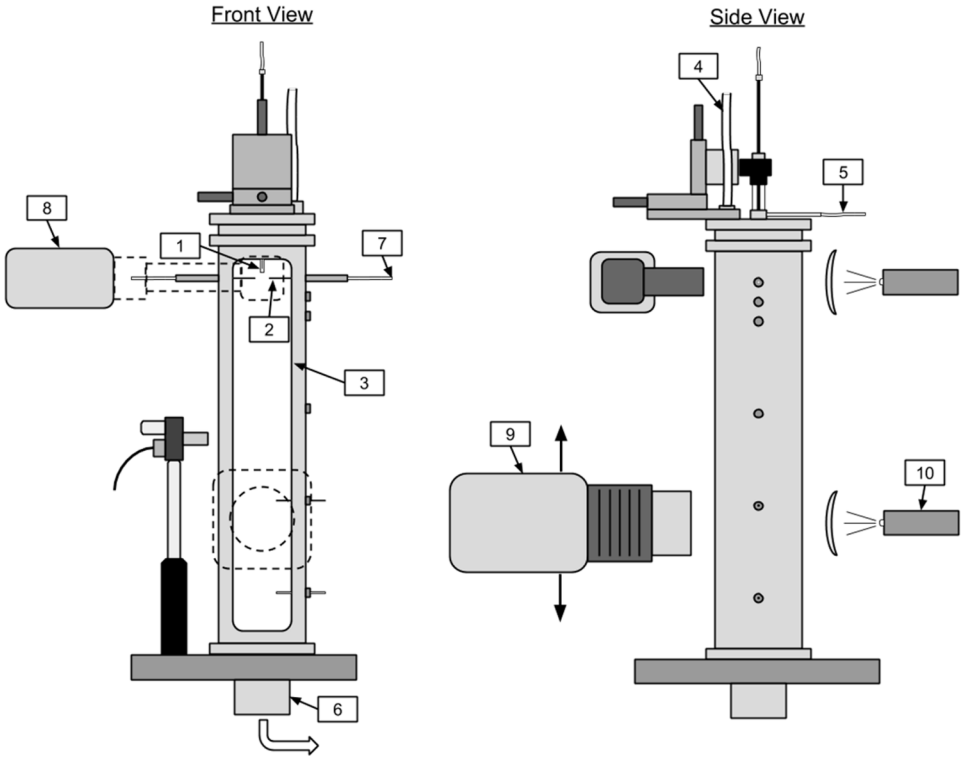

Figure 4. Droplet combustion tower apparatus.

in the tower, the Grashof number is estimated to be 335 while the Reynolds number is approximately 165. Since $Gr/Re^2 < 1$, buoyancy effects are negligible.

Classical liquid droplet combustion theory states that assuming the droplet is fully liquid (and therefore the volume of the droplet is directly coupled with its mass), the rate of decrease in droplet volume is linearly proportional to the diameter of the droplet.[29] By separation of variables and normalization by the initial diameter of the droplet, the governing equation for the droplet diameter as a function of time according to this theory can be written as

$$\frac{D(t)^2}{{D_0}^2} = 1 - K\frac{t}{{D_0}^2} \quad (1)$$

While the experiments of this study do not exactly match the conditions under which the D^2 law is derived, it does provide a metric by which the burning rate of liquid formulations can be characterized: K, the burning rate constant in units of mm^2/s, which increases for faster burning droplets. The droplet diameters and burn times measured are fit to the D^2 law to estimate the burning rate constant by plotting the square of the diameter versus time (both parameters normalized by the square of the initial droplet diameter) and assessing the slope of a linear best fit. Alternately, a far field camera arrangement can capture the entire combustion trajectory instead of droplet diameters measured in flight. By assuming a final droplet diameter at flame extinction and measuring the burn time with the far-field observation, a D^2 law burning rate constant can be estimated without the constraint that the droplet be entirely liquid according to

$$K = \frac{1 - {D_{\text{Extinction}}}^2/{D_0}^2}{t_{\text{Extinction}}/{D_0}^2} \quad (2)$$

Two high speed cameras are used in tandem to observe the droplet combustion, the first ("normalizing") camera (Figure 4, point 8) being used in a static position to image the initial size of the droplets as they pass the methane igniters. The second ("main") camera (point 9) has two configuration options: the first to collect magnified droplet images along the height of the tower and the second ("far-field") configuration to capture the entire combustion trajectory to measure burn times. The magnified configuration consists of the main camera approximately 0.2 m from the tower with a 105 mm lens (F-number 2), 1.7 μs exposure, and lens bellows for magnification. To resolve the edge of the liquid droplet in flight, the camera is aligned with a near-collimated backlight (point 10) and interference filters (0.64% transmittance from 315 to 445 nm and 20% from 700 to 800 nm) to attenuate interference from the flame. By moving the main camera to various positions along the height of the tower, the droplet diameter evolution with time can be plotted. In the far-field configuration, the main camera is approximately 0.75 m from the tower with a 28 mm wide-angle lens (F-number 11) and 2 μs exposure to observe the full trajectory of the droplets over their lifetimes. The burn time is measured based on the time from flame inception upon ignition to flame extinction when the camera no longer detects any emission at maximum gain. Together with an estimated droplet size upon termination, the burn times can also be plotted on a D^2 versus time plot and fit to a classical model to estimate the burning rate constant. The requirement for two burning rate measurement methods is necessitated by the disruptive combustion behavior of the AlBr-laden samples.

In all configurations, the initial droplet size (when passing methane flames) is required to normalize the data and account for any fluctuations in generated droplet size. It is estimated by measuring and averaging the equivalent spherical diameter of the droplet in three image frames nearest the igniter tubes. The

DOI: 10.1021/acs.jpca.5b08580
J. Phys. Chem. A 2015, 119, 11084−11093

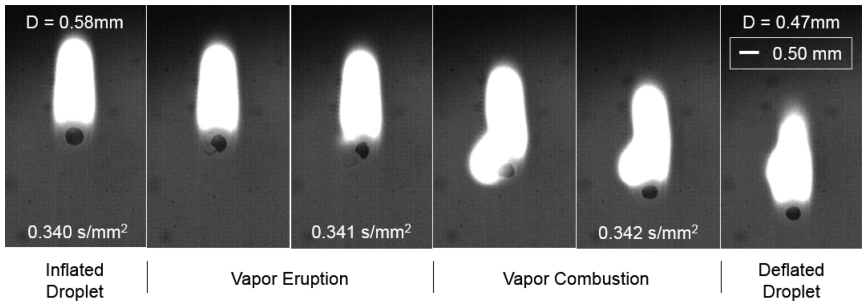

Figure 5. Select video frames of representative 9.7 mM $[AlBrNEt_3]_4$ sample microexplosion event visible by shadowgraph. Liquid-phase droplet visible as dark circle in each frame. Vapor expulsion visible in frames 2 and 3 and its combustion in frames 4 and 5. Time normalized by square of initial droplet diameter = 0.65 mm.

droplet size is approximated by a "plate-shape" ellipsoid whose minor axis is oriented vertically. All video measurements were performed with Vision Research Phantom Camera Control (PCC) software.

In order to capture residual solids remaining after termination of droplet combustion, an SEM substrate was placed in the tower so that the reaction product could impinge on the surface at a location just after combustion terminated.

RESULTS AND DISCUSSION

While hydrocarbon droplets exhibit steady burning until the point of termination, fuel droplets laden with $[AlBrNEt_3]_4$ additive exhibit disruptive burning characterized by cyclical droplet inflations and eruptions or "microexplosions" presumably caused by rapid internal droplet gas release. The 9.7 mM $[AlBrNEt_3]_4$ sample showed on the order of ten microexplosion events (exemplified by Figure 5) over each droplet lifetime, most commonly occurring in the last ~30% of the droplet combustion time. The frequency and intensity of microexplosions appeared to increase with increasing $[AlBrNEt_3]_4$ concentration. In addition in many cases prior to the microexplosion, the droplet size as measured by high magnification video showed swelling of the droplet. As a result of the cyclical droplet inflations and microexplosions, droplet diameters measured in flight for the $[AlBrNEt_3]_4$ additive samples cannot be fit to classical droplet combustion modeled by eq 1. The gas liberation decouples the mass and liquid volume of the droplets, therefore obscuring the direct burning rate constant measurement based on droplet diameter trends.

An alternate method of estimating the fuel burning rate constant was therefore required to quantify the burning rate effect of the $[AlBrNEt_3]_4$ additive in the presence of its disruptive burning. In the far-field camera configuration, the main camera observes the trace of the entire combusting droplet trajectory from which a burn time can be measured. In order to fit a classical droplet burning model to these burn time observations by eq 2, a droplet size upon flame extinction is also required, and therefore characteristic terminations were observed for each sample and are shown in Figure 6. Both the pure solvent and the particulate nAl additive sample terminate explosively at a critical droplet diameter of 0.1 mm. On the other hand, the $[AlBrNEt_3]_4$ additive samples quench more slowly with a solid product remaining. The solid particles were collected to confirm the body observed in the termination video is the same size as the remaining solid particle. It is therefore assumed that all the liquid solvent in the $[AlBrNEt_3]_4$ samples burns, and the critical diameter at flame extinction is taken to be zero.

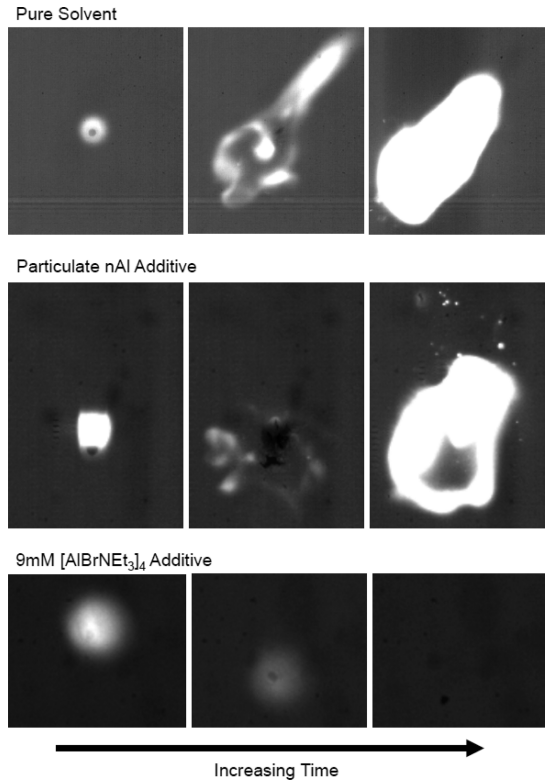

Figure 6. Characteristic termination of droplets composed of pure kerosene and kerosene with nAl additive occurring explosively at 0.1 mm critical droplet diameters; kerosene with $[AlBrNEt_3]_4$ additive quenching slowing as all liquid is consumed.

Using the characteristic termination diameters, the burn times are plotted on the diameter-squared law plot in Figure 7. The classical model expressed by eq 2 can be reasonably fit to these data by linear regression with a $y = 1$ intercept and a burning rate constant thereby estimated by the slope of the fit (Table 1 with 95% confidence interval estimated). These model fits of the burn times (flame extinctions) are shown in Figure 7 as the linear trend lines illustrating the increased slope magnitude of the $[AlBrNEt_3]_4$-laden samples relative to the pure solvent and nAl-laden control samples which indicates an increased burn rate constant caused by the $[AlBrNEt_3]_4$ additive.

The variation of droplet diameters measured in flight for the pure control and nAl particulate samples as functions of normalized time from ignition are shown in Figure 7. Both control samples exhibit disruption-free burning and therefore

DOI: 10.1021/acs.jpca.5b08580
J. Phys. Chem. A 2015, 119, 11084−11093

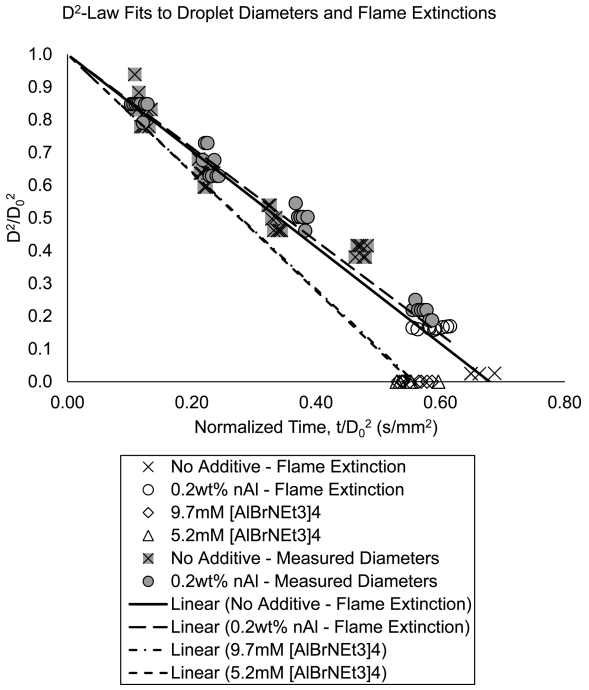

Figure 7. Droplet diameters squared as functions of normalized time from ignition for 80% toluene/20% ethyl with various additives. Linear fits of flame extinction data to classical droplet burning law are shown. Slopes of linear fits are tabulated in Table 1 as burning rate coefficients.

can fit the classical model by eq 1 when the droplet diameters are measured in flight. The resulting burning rate constants, K, are derived from the slopes of linear regression fits and are tabulated in Table 1. The particulate nAl additive shows little to no effect on the burning rate. Pure solvent with triethylamine ligand added was also tested in the same manner to quantify any possible burning rate increase due to the ligand liberation or decomposition. The triethylamine concentration was adjusted to match the concentration of triethylamine contained in the solution containing the $[AlBrNEt_3]_4$ additive assuming all of the ligand was liberated. The ligand control results showed a marginal (~3%) increase in burning rate; however, the combustion was qualitatively disruption-free.

The use of both fitting methods discussed to quantify the burning rate constant of the control samples allows for validation of the flame termination-based method, which employed eq 2 to derive values of K. The resultant K values for the control experiments based on both methods agree reasonably well as evident in Figure 7 and Table 1. The flame termination-based measurement is not compromised by the disruptive nature of the $[AlBrNEt_3]_4$ additive sample combustion, and therefore yields a more accurate estimate for disruptive samples, and shows a 20% increase in burning rate for both concentrations of $[AlBrNEt_3]_4$ additive tested compared to the pure control.

Product particles remaining after the termination of $[AlBrNEt_3]_4$-laden droplets were collected and analyzed via SEM and EDX elemental analysis. A representative micrograph is shown in Figure 8. The volume of a sample droplet released

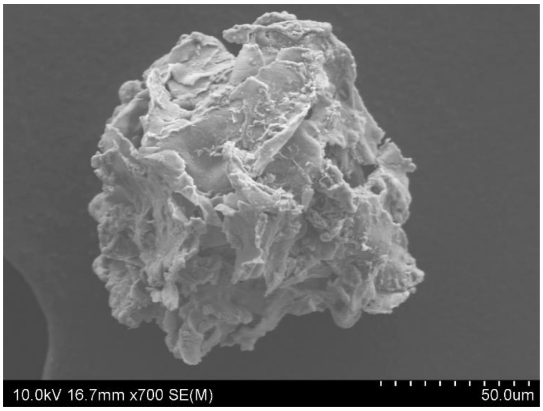

Figure 8. SEM of product particle captured on carbon tape in-flight postcombustion from 9.7 mM $[AlBrNEt_3]_4$ sample.

into the tower is nominally ~9×10^{-4} cm^3. Based on the known aluminum concentration in the $[AlBrNEt_3]_4$-laden droplet, the maximum possible mass of product Al_2O_3 that can be formed from a droplet of this size is ~2.6×10^{-3} g. Assuming the particle captured comprises only Al_2O_3, the maximum density of a 100 μm diameter particle such as that in Figure 8 would therefore be ~0.6 g/cm^3. Assuming the bulk density of Al_2O_3 is 4.0 g/cm^3, this suggests a minimum porosity of the captured particle to be ~85%. Elemental analysis of the outer surface shows an Al:O atomic ratio of ~0.3 (Al_2O_3 = 0.6) with ~5 at. % carbon while an open pore shows an Al:O atomic ratio of ~1.3 with 30 at. % carbon. Noting significant error is inherent in EDX analysis without suitable calibration standards, this result suggests that the particle may not be homogeneous but is likely composed predominantly of Al_2O_3 and carbon species from the highly sooting toluene fuel.

A commonly argued mechanism of droplet microexplosions in multicomponent droplets is that if the boiling points of the components differ enough, the lower boiling point fuel can be superheated when the droplet temperature is driven up by the higher boiling point of the other components.[30−33] This mechanism could potentially explain the explosive terminations of the control samples shown in Figure 6. However, earlier microexplosive events represented by Figure 5 were absent in

Table 1. Experimental Samples with Measured Burning Rate Constants

			burning rate constant based on		
			D^2 trend		time to termination
additive	active Al concn (mM)	percent increase in energy content	K (mm^2/s)	R^2 of fit	K (mm^2/s)
none (control)	none	none	1.41	0.886	1.47 ± 0.10
triethylamine	none	none	1.48	0.956	1.52 ± 0.10
0.2 wt % nAl	50	0.14% (42 kJ/L)	1.37	0.987	1.43 ± 0.14
5.2 mM $[AlBrNEt_3]_4$	21	0.06% (18 kJ/L)	(obscured)	N/A	1.80 ± 0.16
9.7 mM $[AlBrNEt_3]_4$	39	0.11% (33 kJ/L)	(obscured)	N/A	1.79 ± 0.18

DOI: 10.1021/acs.jpca.5b08580
J. Phys. Chem. A 2015, 119, 11084−11093

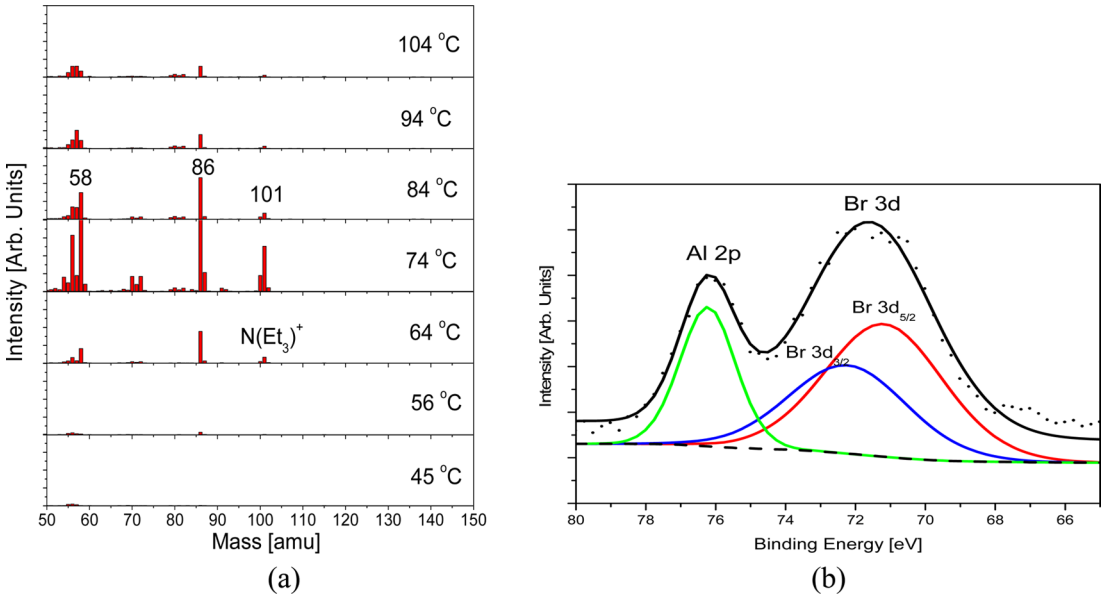

Figure 9. (a) TPR spectra of reaction of $[AlBrNEt_3]_4$ with $^{18}O_2$ at 1×10^{-5} Torr. Peaks match NEt_3 and its known fragmentation pattern (note: the intensity of 58, 86 amu at 74 °C are out of scale). (b) XPS spectra of sample after the reaction showing Al and Br remaining.

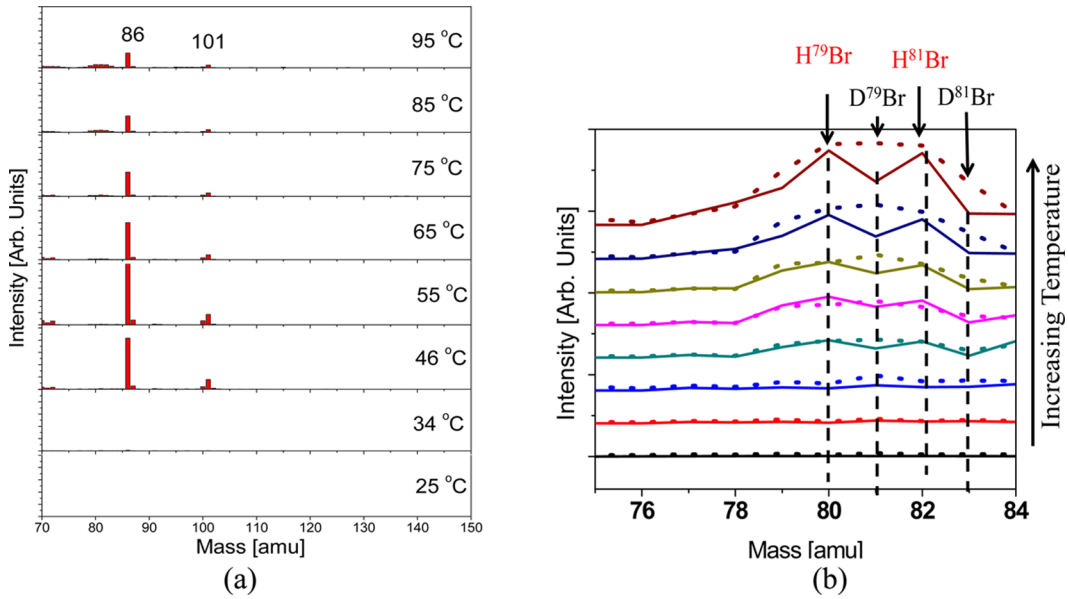

Figure 10. (a) Temperature-programmed reaction spectra of $[AlBrNEt_3]_4$ exposed to D_2O at 1.0×10^{-4} Torr for 1 h. The chamber was the evacuated to 1×10^{-7} Torr, and the TPR was subsequently taken. (b) Comparison of TPR spectra of $[AlBrNEt_3]_4$ exposed to D_2O (dotted line) and not exposed to D_2O (solid line) in the mass 75−84 amu region.

all control runs and therefore are not attributed to this multiple-boiling-point mechanism. Rather, the addition of the $[AlBrNEt_3]_4$ additive was clearly responsible for the internal droplet gas generation, which caused such disruptions. NASA CEA code used to estimate the flame temperature with and without the molar equivalent of aluminum added to toluene fuel (0.0050 mol Al per mole of toluene) results in less than a 10 K increase.[34] This very small increase in heat release cannot account for the observations of disruptive burning.

To further explore the oxidation mechanism of the $[AlBrNEt_3]_4$ additive, temperature-programmed reaction (TPR) experiments of the crystalline solid with O_2 and D_2O oxidants were employed. Since the oxygen concentrations on the fuel side of the spherical diffusion flame are very small, we postulated that the water byproduct of the tol:Et_2O solvent combustion process was diffusing from the flame to the droplet and reacting with the $[AlBrNEt_3]_4$ cluster to generate HBr and Al−O. The control experiments showed that microexplosive gas eruptions were not a result of boiling solvent of liberated triethylamine ligand from the cluster.

TPR experiments were designed to probe the reaction chemistry of the $[AlBrNEt_3]_4$ with oxygen and water by evaluating the evolved gases and solid residues. As a control, crystalline $[AlBrNEt_3]_4$ was first studied by heating the sample in vacuum from 25 to 110 °C with a ramp rate of 10 °C/min. Analysis of the evolved gases by mass spectrometry (Hiden HAL/3F PIC quadruple mass spectrometer) shows that the complex begins to decompose at ∼50 °C to give NEt_3 (101

DOI: 10.1021/acs.jpca.5b08580
J. Phys. Chem. A 2015, 119, 11084−11093

amu), and its fragments (58, 86 amu) as the major products. A similar experiment was conducted in which crystalline $[AlBrNEt_3]_4$ was dosed with 1×10^{-5} Torr isotopically labeled $^{18}O_2$ gas while heating by the same schedule described above. The ^{18}O isotope was used to avoid overlap with other possible products from the reaction. The resulting gases (Figure 9a,b) are virtually identical to the *in vacuo* control TPR experiment showing only NEt_3 and its decomposition fragments. XPS analysis of the resulting white residue showed the presence of Br and Al (III), presumably Al_2O_3. The TPR of the $[AlBrNEt_3]_4$ solid was repeated a third time, dosing instead with 1.0×10^{-4} Torr of D_2O prior to heating to investigate possible reactions induced by the presence of water in the droplets. The resultant spectra show that the major product is still the labile NEt_3 consistent with the previous two experiments with a slightly lower onset temperature (Figure 10a), but closer examination of 75−84 amu mass spectrum region reveals the production of $D^{79}Br$ and $D^{81}Br$ at ∼50 °C (Figure 10b). The presence of $D^{79}Br$ and $D^{81}Br$ from the D_2O exposed sample compared to the nonexposed sample indicates $[AlBrNEt_3]_4$ undergoes a hydrolysis process to generate gaseous DBr while the slightly decreased onset temperature suggests this pathway is kinetically favorable relative to oxidation by O_2 species.

Breaking down these observations, we propose the following simplified step-by-step mechanism, described schematically in Figure 11. Early in the droplet lifetime, the $[AlBrNEt_3]_4$ concentration is considered homogeneous (Figure 11i). In terms of elementary reactions, it is difficult to parse the order at which reaction steps are occurring but in a global sense, combustion of the solvent yields CO_2 and H_2O in the flame region. Upon diffusion of combustion products from the flame to the droplet, reaction of H_2O with $[AlBrNEt_3]_4$, as indicated by the TPR experiments, will lead to the production of HBr gas. Early in the droplet lifetime when it is largely homogeneous, H_2O reaction with $[AlBrNEt_3]_4$ will occur close to the droplet surface, nearest the source of H_2O in the flame. However, liberation of HBr gas will promote convective mixing near the droplet surface and increase transport of water further into the droplet yielding HBr gas within the liquid, exemplified by the mixing evident upon gas generation in Figure 12. This

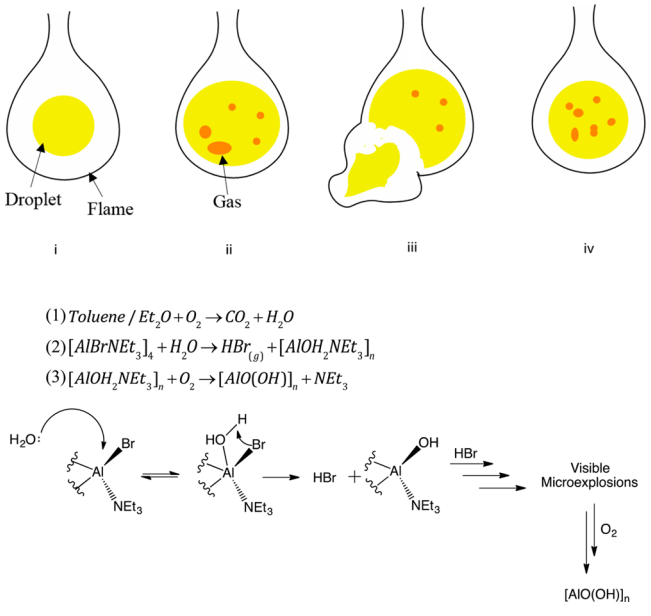

Figure 11. Proposed reaction of $[AlBrNEt_3]_4$ dissolved in a mixture of toluene/Et_2O exposed to an O_2 atmosphere and burned (i). The combustion of the solvents leads to the formation of $CO_{2(g)}$ and $H_2O_{(g)}$ (1). The H_2O contributes the oxidation of Al^{1+}, the formation of $HBr_{(g)}$, and the expulsion of $NEt_{3(l)}$ (ii) (2) leading to visible microexplosions (iii). This gas liberation and expulsion repeats (iv) and leads to increased mixing of the droplet and its contents with the oxidizer-rich surroundings leading to the formation of $[AlO(OH)]_n$ products (3).

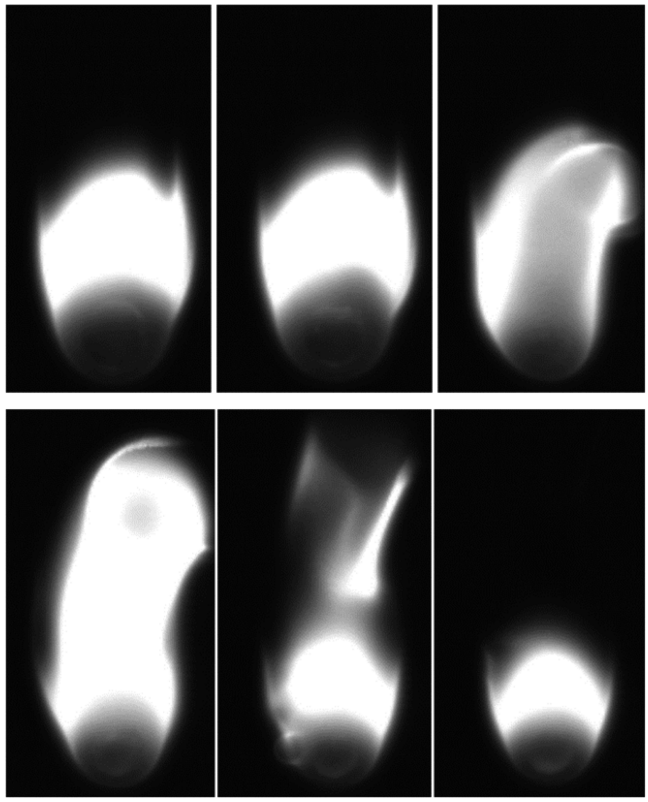

Figure 12. Gas generation in AlBr-laden droplet. Top row: inflated droplet releasing gas. Bottom row: deflated droplet after gas release with flame perturbation. Image period = 234 μs.

enhanced mixing should promote faster $[AlBrNEt_3]_4$ decomposition and formation of HBr. At high enough concentrations, the gas nucleates to bubbles and results in the microexplosions observed (Figures 6, 11 (ii and iii), and 12). These gas release events transport more fuel to the flame region and affect the burning rate (Figure 11 (iii)). The droplet then returns to a deflated droplet form until the next visible event (Figure 11 (iv)). This process is repeated throughout the remainder of the droplet lifetime, until the solvent flame extinguishes where the major product left is alumina (according to XPS).

The mechanism proposed is supported by the fewer incidences of visible microexplosions in less concentrated samples, wherein less $[AlBrNEt_3]_4$ is available for reaction and HBr liberation, and the observation of microexplosions only in the last ∼30% of the droplet burn time. Since gas phase diffusion of water to the droplet will occur much faster than its condensed phase diffusion within the droplet, the time scale of this process can be conservatively estimated by considering the rate of diffusion of water from the edge to the inner region of the droplet in the absence of convective mixing. Assuming that

DOI: 10.1021/acs.jpca.5b08580
J. Phys. Chem. A 2015, 119, 11084−11093

a 0.1 mm diameter sphere of HBr gas is ample to produce the first microexplosion, 1.8×10^{-11} mol of water is required to diffuse into the droplet and react with $[AlBrNEt_3]_4$. Considering a static 0.5 mm diameter droplet saturated with 0.33% water at its surface with a binary diffusion coefficient of 10^{-5} cm^2/s, the mean Fickian diffusion flux of water would be $\sim 6 \times 10^{-4}$ $mol/(m^2\ s)$, assuming a linear concentration gradient within the droplet. This then yields an approximate transport time for a microexplosion of ~150 ms and presumably is a conservative estimate since we are neglecting any convection effects. Considering a total burn time is ~250 ms, this supports the proposed mechanism wherein initial HBr liberation is produced by water diffusing within the droplet. In summary, the production of HBr causes bubble nucleation and droplet deformation to allow for increased mixing of the droplets with the oxidizing environment and thus increased reactant transport and burning rate.

CONCLUSIONS

The mechanism of combustion enhancement of a soluble molecular $[AlBrNEt_3]_4$ cluster additive in liquid fuel has been studied in single droplet combustion experiments. The $[AlBrNEt_3]_4$ additive increases the burning rate constant of a toluene−diethyl ether fuel mixture by 20% in a room temperature oxygen environment with 39 mM of active aluminum additive (approximately 0.16 wt %). The primary mechanism for enhancement seems to be liquid-phase internal droplet gas generation leading to disruptive burning. Similar experiments with nano-aluminum showed no discernible enhancement at these low concentrations. While the $[AlBrNEt_3]_4$ additive did not contain enough Al at these concentrations to appreciably increase the calorific value of the fuel, this study shows that the soluble architecture of the Al-based additive contributes a novel mechanism to increase the burning rate of hydrocarbon fuels, providing significantly more reactivity than its particulate nano-aluminum counterpart.

AUTHOR INFORMATION

Corresponding Author

*(M.R.Z.) E-mail: mrz@umd.edu.

Notes

The authors declare no competing financial interest.

ACKNOWLEDGMENTS

This work was made possible from the support form an Air Force Office of Scientific Research MURI grant and the Defense Threat Reduction Agency.

REFERENCES

(1) Yetter, R. A.; Risha, G. A.; Son, S. F. Metal Particle Combustion and Nanotechnology. *Proc. Combust. Inst.* **2009**, *32*, 1819−1838.
(2) Dreizin, E. L. Metal-Based Reactive Nanomaterials. *Prog. Energy Combust. Sci.* **2009**, *35*, 141−167.
(3) Choi, S. U. S.; Eastman, J. A. Enhancing Thermal Conductivity of Fluids with Nanoparticles. *ASME Int. Mech. Eng. Congr. Expo.*, 1995.
(4) Kao, M. J.; Ting, C. C.; Lin, B. F.; Tsung, T. T. Aqueous Aluminum Nanofluid Combustion in Diesel Fuel. *J. Test. Eval.* **2008**, *36*, 100579.
(5) Tyagi, H.; Phelan, P. E.; Prasher, R.; Peck, R.; Lee, T.; Pacheco, J. R.; Arentzen, P. Increased Hot-Plate Ignition Probability for Nanoparticle-Laden Diesel Fuel. *Nano Lett.* **2008**, *8*, 1410−1416.
(6) Mehta, R. N.; Chakraborty, M.; Parikh, P. A. Nanofuels: Combustion, Engine Performance, and Emissions. *Fuel* **2014**, *120*, 91−97.
(7) Sajith, V.; Sobhan, C. B.; Peterson, G. P. Experimental Investigations on the Effects of Cerium Oxide Nanoparticle Fuel Additives on Biodiesel. *Adv. Mech. Eng.* **2010**, *2*, 581407.
(8) Sarvestany, N. S.; Farzad, A.; Ebrahimnia-Bajestan, E.; Massoud, M. Effects of Magnetic Nanofluid Fuel Combustion on the Performance and Emission Characteristics. *J. Dispersion Sci. Technol.* **2014**, *35*, 1745−1750.
(9) Singh, N.; Bharj, R. S. Effect of CNT-Emulsified Fuel on Performance Emission and Combustion Characteristics of Four Stroke Diesel Engine. *Int. J. Curr. Eng. Technol.* **2015**, *5*, 477−485.
(10) Van Devener, B.; Anderson, S. L. Breakdown and Combustion of JP-10 Fuel Catalyzed by Nanoparticulate CeO_2 and Fe_2O_3. *Energy Fuels* **2006**, *20*, 1886−1894.
(11) Allen, C.; Mittal, G.; Sung, C. J.; Toulson, E.; Lee, T. An Aerosol Rapid Compression Machine for Studying Energetic-Nanoparticle-Enhanced Combustion of Liquid Fuels. *Proc. Combust. Inst.* **2011**, *33*, 3367−3374.
(12) Sabourin, J. L.; Dabbs, D. M.; Yetter, R. A.; Dryer, F. L.; Aksay, I. A. Functionalized Graphene Sheet Colloids for Enhanced Fuel/Propellant Combustion. *ACS Nano* **2009**, *3*, 3945−3954.
(13) Sabourin, J. L.; Yetter, R. A.; Asay, B. W.; Lloyd, J. M.; Sanders, V. E.; Risha, G. A.; Son, S. F. Effect of Nano-Aluminum and Fumed Silica Particles on Deflagration and Detonation of Nitromethane. *Propellants, Explos., Pyrotech.* **2009**, *34*, 385−393.
(14) Sabourin, J. L.; Yetter, R. A.; Parimi, V. S. Exploring the Effects of Nanostructured Particles on Liquid Nitromethane Combustion. *J. Propul. Power* **2010**, *26*, 1006−1015.
(15) McCown, K. W.; Petersen, E. L. Effects of Nano-Scale Additives on the Linear Burning Rate of Nitromethane. *Combust. Flame* **2014**, *161*, 1935−1943.
(16) Gan, Y.; Qiao, L. Radiation-Enhanced Evaporation of Ethanol Fuel Containing Suspended Metal Nanoparticles. *Int. J. Heat Mass Transfer* **2012**, *55*, 5777−5782.
(17) Gan, Y.; Qiao, L. Optical Properties and Radiation-Enhanced Evaporation of Nanofluid Fuels Containing Carbon-Based Nanostructures. *Energy Fuels* **2012**, *26*, 4224−4230.
(18) Javed, I.; Baek, S. W.; Waheed, K.; Ali, G.; Cho, S. O. Evaporation Characteristics of Kerosene Droplets with Dilute Concentrations of Ligand-Protected Aluminum Nanoparticles at Elevated Temperatures. *Combust. Flame* **2013**, *160*, 2955−2963.
(19) Javed, I.; Baek, S. W.; Waheed, K. Effects of Dense Concentrations of Aluminum Nanoparticles on the Evaporation Behavior of Kerosene Droplets at Elevated Temperatures: The Phenomenon of Microexplosion. *Exp. Therm. Fluid Sci.* **2014**, *56*, 33−44.
(20) Javed, I.; Baek, S. W.; Waheed, K. Autoignition and Combustion Characteristics of Heptane Droplets with the Addition of Aluminum Nanoparticles at Elevated Temperatures. *Combust. Flame* **2015**, *162*, 191−206.
(21) Tanvir, S.; Qiao, L. Effect of Addition of Energetic Nanoparticles on Droplet-Burning Rate of Liquid Fuels. *J. Propul. Power* **2015**, *31*, 408−415.
(22) Gan, Y.; Lim, Y. S.; Qiao, L. Combustion of Nanofluid Fuels with the Addition of Boron and Iron Particles at Dilute and Dense Concentrations. *Combust. Flame* **2012**, *159*, 1732−1740.
(23) Gan, Y.; Qiao, L. Evaporation Characteristics of Fuel Droplets with the Addition of Nanoparticles under Natural and Forced Conventions. *Int. J. Heat Mass Transfer* **2011**, *54*, 4913−4922.
(24) Javed, I.; Baek, S. W.; Waheed, K. Evaporation Characteristics of Heptane Droplets with the Addition of Aluminum Nanoparticles at Elevated Temperatures. *Combust. Flame* **2013**, *160*, 170−183.
(25) Gan, Y.; Qiao, L. Combustion Characteristics of Fuel Droplets with Addition of Nano and Micron-Sized Aluminum Particles. *Combust. Flame* **2011**, *158*, 354−368.
(26) Timms, P. Chemistry of Boron and Silicon Subhalides. *Acc. Chem. Res.* **1973**, *6*, 118−123.

DOI: 10.1021/acs.jpca.5b08580
J. Phys. Chem. A 2015, 119, 11084−11093

(27) Tacke, M.; Schnöckel, H. Metastable Aluminum Chloride, AlCl, as a Solid and in Solution. *Inorg. Chem.* **1989**, *28*, 2895−2896.
(28) Mocker, M.; Robl, C.; Schnöckel, H. Donor-Stabilized Aluminum(I) Bromide. *Angew. Chem., Int. Ed. Engl.* **1994**, *33*, 1754−1755.
(29) Godsave, G. A. E. Studies of the Combustion of Drops in a Fuel Spray—the Burning of Single Drops of Fuel. *Symp. (Int.) Combust., [Proc.]* **1953**, *4*, 818−830.
(30) Law, C. K. Internal Boiling and Superheating in Vaporizing Multicomponent Droplets. *AIChE J.* **1978**, *24*, 626−632.
(31) Law, C. K. Recent Advances in Droplet Vaporization and Combustion. *Prog. Energy Combust. Sci.* **1982**, *8*, 171−201.
(32) Wang, C. H.; Liu, X. Q.; Law, C. K. Combustion and Microexplosion of Freely Falling Multicomponent Droplets. *Combust. Flame* **1984**, *56*, 175−197.
(33) Makino, A.; Law, C. K. On the Controlling Parameter in the Gasification Behavior of Multicomponent Droplets. *Combust. Flame* **1988**, *73*, 331−336.
(34) McBride, B. J.; Gordon, S. Computer Program for Calculation of Complex Chemical Equilibrium Compositions and Applications, II: Users Manual and Program Description, NASA RP-1311, 1996.

DOI: 10.1021/acs.jpca.5b08580
J. Phys. Chem. A 2015, 119, 11084−11093